https://doi.org/10.5194/egusphere-2025-6470
Preprint. Discussion started: 25 February 2026

Elucidating CO_2 accumulation and dispersion in a semi-enclosed bay industrial park using Lidar and WRF-GHG modelling

Daihao Yu[1,2,4], Qiuwei Xia[1,2,4], Saifen Yu[1,2,4], Yixiang Chen[1,2,4], Keyi Xu[1,2], Haobin Han[1,2,5], Jianjun Guo[1,2], Kexin Guo[1,2,5], Jiadong Hu[1,2,5], Zhen Zhang[1,2,4], Jing Cai[1,2], Yuanjian Yang[1,2], Haiyun Xia[1,2,3,4,5]

[1] State Key Laboratory of Climate System Prediction and Risk Management (CPRM), NUIST, Nanjing 210044, China
[2] School of Atmospheric Physics, Nanjing University of Information Science and Technology, Nanjing 210044, China
[3] School of Earth and Space Science, University of Science and Technology of China, Hefei 230026, China
[4] National Center of Carbon Metrology (Fujian), Nanping 353000, China
[5] Institute of Lidar Technology, GuangZai Co. Ltd., Hangzhou 310005, China

Correspondence to: Zhen Zhang (zhenzhang@nuist.edu.cn) , Haiyun Xia (hsia@ustc.edu.cn)

Abstract. Industrial parks represent critical nodes in the global carbon cycle and thus require accurate monitoring and modelling to support effective carbon management. Although satellite observations, ground-based measurements, and numerical modelling frameworks have been widely utilized, these approaches inherently struggle to simultaneously achieve high temporal and spatial resolution. In this study, high-resolution Lidar is integrated with the Weather Research and Forecasting model coupled with greenhouse gas fluxes (WRF-GHG) modelling to comprehensively diagnose the CO_2 accumulation–dispersion dynamics and their driving mechanisms within the Luoyuan Bay industrial park. The comprehensive analysis reveals a distinctive diurnal pattern of CO_2, characterized by nighttime accumulation and daytime dispersion. Lidar observations indicate that stable atmospheric conditions and valley terrain synergistically cause CO_2 to accumulate in low-lying areas at night, with concentrations exceeding 700 ppm. During daytime, strengthened southeasterly sea breezes and intensified turbulence promote its dispersion to the northwest and vertical uplift, reducing concentrations to 500-550 ppm. A significantly negative correlation between CO_2 concentration and wind speed is also confirmed. While the WRF-GHG model reproduces the overall temporal variation, it systematically underestimates CO_2 levels (420-460 ppm). The discrepancy is attributed to the limited spatial resolution of the emission inventory and the model's inherent constraints in capturing terrain–wind field interactions within the bay. This study highlights the unique capabilities of coherent differential absorption Lidar, elucidates the key limitations of current modelling approaches, and provides a robust scientific basis for refining carbon verification systems and enhancing the performance of regional carbon models.

1 Introduction

Since the Industrial Revolution, the continuous rise in greenhouse gas concentrations driven by anthropogenic activities has become a significant perturbation to the global climate system. Global surface temperatures have increased by approximately 1.1°C compared to pre-industrial levels, with the cumulative emissions of CO_2 being the key driver of this change (IPCC 2023).

https://doi.org/10.5194/egusphere-2025-6470
Preprint. Discussion started: 25 February 2026

As the primary greenhouse gas, the continuous emission of CO_2 exerts a profound impact on global climate change. In recent years, global CO_2 emissions have continued to grow, with the industrial sector accounting for 28.5% of the total in 2024 (Deng et al., 2025). As the world's largest carbon emitter and home to the largest manufacturing sector, China's CO_2 emissions originate primarily from industrial sources. Monitoring and regulating industrial CO_2 emissions is of exemplary significance for advancing the low-carbon transition of the global industrial system and deepening cooperation on climate governance.

Currently, industrial CO_2 emissions monitoring technologies mainly include in situ monitoring and remote sensing monitoring methods. In situ instrumental monitoring conducts real-time measurement of atmospheric CO_2 concentrations via fixed-site online devices but struggles to effectively cover large-scale areas (Gurney et al., 2002). Remote sensing monitoring is divided into satellite remote sensing and ground-based remote sensing. Satellite remote sensing utilizes satellites such as OCO-2/3 (Taylor et al., 2023; Wang et al., 2025), GOSAT2 (Imasu et al., 2023; Zhang et al., 2024), DQ-1 (Han et al., 2024), and GF-5 (Ye et al., 2022) to monitor regional or global CO_2 column concentration distributions. For instance, spaceborne IPDA Lidar technology is used to estimate the diurnal variation characteristics of CO_2 emissions from thermal power plants (Zhang et al., 2025), and synergistic observation of pollutant gases is employed to enhance the tracking capability of power plant emissions (Fan et al., 2025). However, satellite remote sensing still faces limitations such as insufficient valid data at specific locations and insensitivity to surface concentration changes (Shan et al., 2019). In terms of ground-based remote sensing, Fourier transform infrared spectrometers (FTIR) of the Total Carbon Column Observing Network (TCCON) provide calibration benchmarks and high-precision validation for satellite data(Yang et al., 2020; Lu et al., 2025). In recent years, differential absorption Lidar (DIAL) technology has been widely applied in ground-based observation platforms for monitoring volcanic and industrial source emissions (Queiβer et al., 2016; Yue et al., 2022; Stroud et al., 2023). DIAL can provide high spatiotemporal resolution CO_2 concentration and synchronous wind field data within a range of several kilometres, deeply revealing regional CO_2 distribution characteristics, vertical profiles, and transport processes (Yu et al., 2024), which holds great value for the long-term monitoring of industrial CO_2 emissions.

Regional atmospheric transport models serve as essential tools for understanding and quantifying the spatiotemporal distribution of CO_2 emissions. Among them, the Weather Research and Forecasting model coupled with greenhouse gas fluxes (WRF-GHG), as a specialized extended version of the WRF-Chem model, can simultaneously simulate meteorological fields and three-dimensional concentration distributions of multiple greenhouse gases by coupling the Vegetation Photosynthesis and Respiration Model (VPRM, Ahmadov et al., 2007), enabling the separation and tracking of different source and sink processes such as anthropogenic emissions, biogenic fluxes, oceanic exchange, and biomass burning(Ahmadov et al., 2007; Beck et al., 2013). The WRF-GHG model adopts a tracer method, decomposing the total CO_2 concentration into multiple independent components. It can not only capture large-scale transport processes but also accurately simulate complex dispersion characteristics caused by the interaction between local emissions and terrain at the urban scale (1-3 km resolution) (Zhao et al., 2019; Bisht et al., 2023). Application studies of this model in regions such as Berlin (Zhao et al., 2019), Munich (Zhao et al., 2023), Brazil(Alberti et al., 2024), Tokyo (Bisht et al., 2025), and the Beijing-Tianjin-Hebei region of China (Dong et al., 2021; Callewaert et al., 2024) have shown that high-resolution WRF-GHG simulations can effectively identify

https://doi.org/10.5194/egusphere-2025-6470
Preprint. Discussion started: 25 February 2026

industrial emission hotspots, quantify the contribution ratios of different sectors (energy, industry, transportation, residential), and verify the accuracy of emission inventories through synergistic analysis with ground-based FTIR observations and satellite remote sensing. Although DIAL technology provides high spatiotemporal resolution small-scale CO_2 concentration distribution and vertical profile information (Hu et al., 2026; Yu et al., 2026), and the WRF-GHG model can characterize atmospheric transport processes under complex terrain, no studies have yet organically combined them.

This study focuses on Luoyuan Bay, located along the northeastern coast of Fuzhou City, Fujian Province, China. The region features a typical semi-enclosed bay topography. Its unique geographical conditions, combined with intensive industrial emissions, make it an ideal case for studying CO_2 accumulation and dispersion mechanisms under the combined effect of complex underlying surfaces and high-intensity point sources. A comprehensive observation and simulation analysis over this region is conducted by integrating coherent DIAL with the WRF-GHG model. The coherent DIAL can simultaneously acquire high spatiotemporal resolution CO_2 concentration and three-dimensional wind field data. This offers unique advantages for accurately capturing emission dynamics. The WRF-GHG model, by contrast, can characterize transport processes under complex terrain and quantify contributions from different sources and sinks. The organic combination of the two provides a new research approach. It enables in-depth analysis of the spatiotemporal evolution of industrial CO_2 under the influence of special terrain and land-sea circulation. It also supports systematic evaluation of the model's simulation performance and limitations in such complex scenarios. Based on these findings, this study aims to: (1) employ DIAL observations to characterize CO_2 accumulation under stable meteorological conditions and daytime dispersion mechanisms in industrial parks within semi-enclosed bays; (2) evaluate the simulation capability of the WRF-GHG model for high-intensity point source emissions in complex terrain and analyze its sources of bias; (3) clarify the comprehensive impacts of terrain and land-sea breeze circulation on pollutant transport and dispersion.

This work is structured as follows: Section 2 introduces the data and methods used, including DIAL observation configuration, WRF-GHG model setup, and driving data. Section 3 presents results from Lidar observations and model simulations. It includes a comparative analysis of the two, with a focus on CO_2 accumulation and dispersion phenomena and their driving factors. Section 4 summarizes the main conclusions and provides an outlook on future research directions.

2. Materials and Methods

2.1 Study Area

This study selected Luoyuan Bay (119.61976°E, 26.47362°N) as the study area. It lies along the northeastern coast of Fuzhou City, Fujian Province. Luoyuan Bay is a typical semi-enclosed deep-water bay. The region experiences a subtropical monsoon climate. The bay is surrounded by mountains on all sides. Only a 2 km-wide opening in the east connects it to the East China Sea (Wang et al., 2018). The industrial layout of Luoyuan Bay is centered on heavy industries: iron and steel, energy, chemical engineering, and machinery manufacturing. The southern bank is home to thermal power plants and petrochemical projects,

https://doi.org/10.5194/egusphere-2025-6470
Preprint. Discussion started: 25 February 2026

while the northern bank is dominated by iron and steel metallurgical enterprises. These intensive industrial emissions interact with the bay's unique terrain. This further worsens local air pollution.

2.2 Lidar Observation Method

Since 14 February 2025, a 1.57-μm coherent DIAL has been deployed on the rooftop of a 30 m high building at an iron and steel company near the northern coast of Luoyuan Bay. It conducted long-term observations of the industrial park in northern Luoyuan Bay.

The Lidar has a maximum detection range of 3 km, a range resolution of 120 m, and a time resolution of 1 min. It can simultaneously measure CO_2 concentrations and wind fields. The CO_2 measurement accuracy has been confirmed in prior validation, measured at a background concentration of 463 ppm, showing a mean error of 2.05 ppm and a standard deviation of 7.18 ppm. When compared to an optical cavity ring-down spectrometer, the correlation coefficient reaches 0.91 and the root-mean-square error (RMSE) is 5.24 ppm (Yu et al., 2024). For wind field measurements, the RMSE of horizontal wind speed is less than 0.6 m s^{-1}, the RMSE of wind direction is less than 11°, and the vertical wind speed measurement accuracy is 0.2 m s^{-1} (Yuan et al., 2022) In previous work, the same type of Lidar has successfully detected the transport and dispersion of CO_2 in Nanping and Pucheng industrial parks(Yu et al., 2026).

The Lidar performed synchronous detection of CO_2 concentrations and wind fields over the main area of the northern industrial park at a fixed elevation angle of 10°, an azimuth range of 306° to 16°, and an azimuth step of 2°. A complete scan takes approximately 52 minutes. The scanning range and Lidar location are shown in Fig. 1a. In addition, temperature, humidity, and pressure sensors were deployed around the Lidar installation site to record the park's temperature, humidity, and atmospheric pressure data.

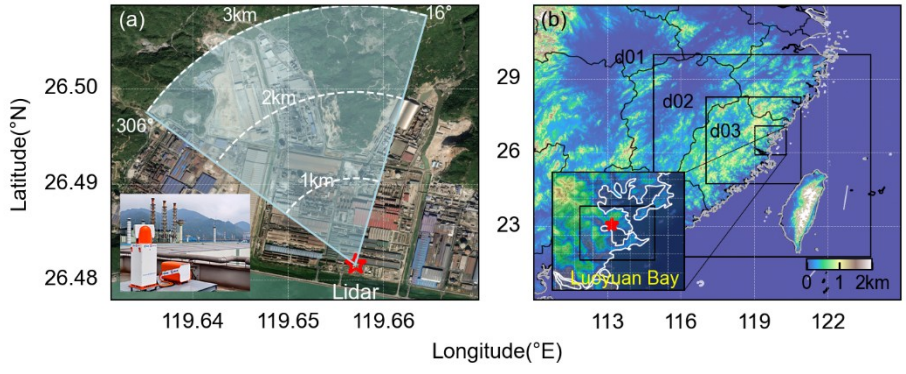

Figure 1. (a) Lidar scanning coverage spans azimuth angles from 306° to 16°; The lower left corner depicts the lidar in field operation; (b) Schematic diagram of the three-layer nested simulation domains in WRF-GHG, with the black rectangular box indicating the location of Luoyuan Bay and the red five-pointed star marking the Lidar installation site. Map source: Microsoft Bing Maps 2026.

https://doi.org/10.5194/egusphere-2025-6470
Preprint. Discussion started: 25 February 2026

2.3 WRF-GHG simulation

The Weather Research and Forecasting model coupled with Chemistry version 4.5.0 (Shi et al., 2024)was employed in this study. The chem_opt = 17 option was selected to configure the WRF-GHG model for simulating CO_2 emissions and atmospheric transport. WRF-GHG is an Eulerian atmospheric transport model. It can simultaneously simulate the three-dimensional concentration distributions of trace gases (e.g., CO_2, CH_4 and CO) and meteorological fields at each time step. The model treats greenhouse gases as passive tracers, considering only their physical transport and mixing processes in the atmosphere while ignoring chemical reaction mechanisms. It classifies greenhouse gases into multiple tracer fields based on their sources (e.g., anthropogenic emissions, biogenic sources, and biomass burning), with flux data provided via external inventories or online calculations.

The simulation period of this study is from 5 March to 31 March 2025, with three nested domains configured. The parent domain (d01) consists of 104 × 104 grid cells with a resolution of 9 km × 9 km, covering southeastern China (Fig. 1b). The second domain (d02) contains 133 × 133 grid cells with a resolution of 3 km × 3 km, covering Fujian Province, China. The innermost domain (d03) is composed of 130 × 130 grid cells with a resolution of 1 km × 1 km, focusing on Luoyuan County, Fujian Province. Fifty-one vertical levels are set from the surface up to 50 hPa, with 30 enhanced levels in the 0–3 km range. Referring to the work of Callewaert et al. (2025), the microphysical parameters configured for the WRF-GHG simulation are presented in Table 1.

Table 1. Microphysical parameters configured for the WRF-GHG simulation

Physics Scheme	Scheme name	Option
Microphysics	Morrison 2-moment	10
Longwave radiation	RRTMG	4
Shortwave radiation	RRTMG	4
Planetary boundary layer	YSU	1
Surface layer	Eta similarity	1
Cumulus	Grell 3D Ensemble	5
Land surface	Unified Noah Land Surface Model	2

The European Centre for Medium-Range Weather Forecasts (ECMWF) fifth-generation global climate reanalysis product (ERA5, 0.25° × 0.25°, Hersbach et al., 2023a, b) was used as meteorological forcing data. The Copernicus Atmosphere Monitoring Service (CAMS) global greenhouse gas forecasts dataset (Agustí-Panareda et al., 2022) provided the required CO_2 initial and boundary conditions for the model. CAMS produces daily global forecasts for the two main long-lived greenhouse gases. This dataset consists of 5-day high-resolution forecasts of CO_2 and CH_4, with additional CO and meteorological parameters relevant to the CAMS greenhouse gas forecasting system. We selected the three-hourly interval products from the first day of each daily forecast, with a spatial resolution of 0.1° and 137 vertical model levels. Anthropogenic CO_2 emissions

https://doi.org/10.5194/egusphere-2025-6470
Preprint. Discussion started: 25 February 2026

were derived from the Emissions Database for Global Atmospheric Research database (EDGAR_2024_GHG, Crippa et al. 2024) for the year 2023.

The biogenic CO_2 fluxes required by WRF-GHG were calculated online using the VPRM (Ahmadov et al., 2007). The model utilized 100-meter resolution land cover data from The Copernicus Land Monitoring Service (CLMS) for 2019, specifically the "Land Cover 2015-2019 (raster 100 m), global, annual - version 3" dataset as essential land cover inputs for VPRM. The enhanced vegetation index (EVI) and land surface water index (LSWI), which are critical for photosynthetic activity and ecosystem respiration calculations, were extracted from Moderate Resolution Imaging Spectroradiometer (MODIS) satellite observations using the pyVPRM (Glauch et al., 2025). Biomass burning emissions were obtained from the CAMS Global Fire Assimilation System (GFAS) data (Kaiser et al., 2012). For the CO_2 ocean flux component, carbon dioxide partial pressure (pCO_2) and sea-air CO_2 flux data were sourced from the JMA Ocean CO_2 Map dataset(Iida et al., 2021) provided by the Japan Meteorological Agency (JMA), using the 10-year (2015-2024) average values.

3. Observation Results

3.1 CO_2 Lidar Observation Results

Figure 2 presents the Lidar detection results from 14 February to 6 April 2025 local time (LT; UTC+8). To accurately assess the impact of industrial park emissions on the surrounding environment, a forested area within the Lidar's azimuth range of 315°–320° and radial distance of 2.7–3 km was selected as the downwind site. Dominantly composed of evergreen broad-leaved forests, this area maintains a high photosynthetic rate year-round. With a vertical elevation difference of approximately 450 m from the Lidar installation, it effectively reflects the concentration level of pollutants after dispersion. Emission source data were obtained from the park's emission area within the Lidar's detection range, i.e., the industrial production zone with an azimuth of 315°–4° and a radial distance of 500–1500 m. Valid data were selected as those with the carrier-to-noise ratio (CNR) > -35 dB within the scanning range for statistical analysis.

During the entire study period, the average CO_2 concentration at the emission source was 578 ppm, while the average concentration at the downwind site was 487 ppm, with a difference of 91 ppm (Fig. 2a). Meanwhile, the mean wind speed was 2.7 m s^{-1}. During the observation period, there were multiple episodes of high nighttime CO_2 concentrations exceeding 700 ppm in the park, such as 1–3 March, 9–15 March and 24–27 March. From March 24 to 27, the daily maximum concentration of the emission source exceeded 900 ppm on each day. The occurrence of this peak is highly consistent with the stable meteorological conditions where wind speeds in the park are below 2 m s^{-1}. At night, the atmospheric dispersion capacity is extremely weak, and CO_2 continuously emitted by factories accumulates inside the park, making it difficult to disperse outward, thus resulting in high overall CO_2 concentrations in the park.

Notably, the park's CO_2 concentrations exhibit distinct diurnal characteristics: they remain high from 21:00 to 09:00 next day, gradually decrease from 10:00 to 15:00, and reach a diurnal minimum at 15:00. In Fig. 2b, the downwind site shows smaller

https://doi.org/10.5194/egusphere-2025-6470
Preprint. Discussion started: 25 February 2026

concentration fluctuations, with afternoon concentrations slightly higher than nighttime levels. This difference is closely related to changes in land-sea breeze circulation and turbulence.

Analysis combined with the wind rose plot at the emission source (Fig. 2c) shows that after sunrise during the daytime, surface heating intensifies, and turbulence activity increases. Meanwhile, as a semi-enclosed bay, Luoyuan Bay exhibits a prominent land-sea breeze effect: prevailing southeasterly winds transport high concentration of CO_2 from industrial emissions to the downwind site in the north-west. However, the surrounding mountainous terrain impedes horizontal dispersion, forcing part of the CO_2 to lift vertically, which further promotes pollutant dilution. In addition, the photosynthesis of forests enters an active period during the daytime, and the absorption of CO_2 partially offsets the increment of industrial emissions, preventing a sharp rise in concentrations at the downwind site.

At night, by contrast, land breezes prevail, the atmosphere becomes stably stratified, and turbulence is suppressed. Wind speeds often drop below 2 m s^{-1}, resulting in calm winds at night. Meanwhile, vegetation releases CO_2 through respiration, which overlaps with pollutants continuously emitted by factories. Coupled with the specific influence of the valley terrain, CO_2 continuously accumulates in the near-surface layer, forming a pattern of high nighttime CO_2 concentrations.

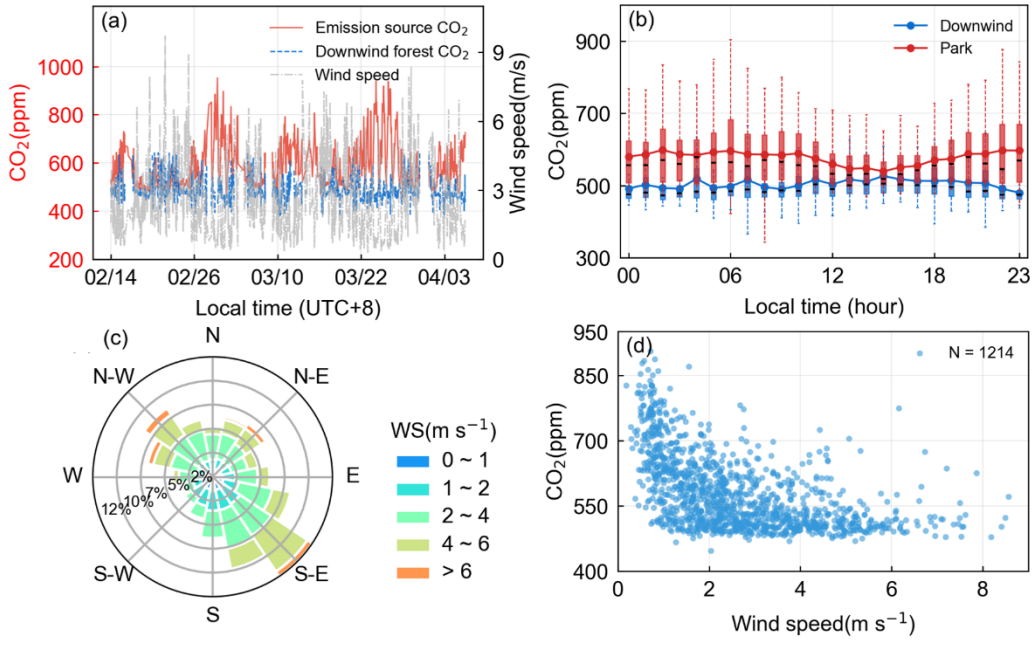

Figure 2. (a) Time series of CO_2 concentrations at the emission source and downwind point, along with wind speed measurements, from 14 February to 6 April 2025 (LT; UTC+8), as detected by the Lidar; (b) diurnal variations in CO_2 concentrations at the emission source and downwind point; (c) wind rose diagram at the emission source; (d) relationship between wind speed and CO_2 concentration within the industrial park area.

Figure 2d depicts the relationship between wind speed and CO_2 concentration within the entire park (Lidar detection range: 0–2 km). The two show a significant negative correlation: As wind speed decreases, atmospheric dispersion capacity weakens,

https://doi.org/10.5194/egusphere-2025-6470
Preprint. Discussion started: 25 February 2026

and the more likely CO_2 emitted by the park is to accumulate in low-lying valley areas, forming localized high concentration zones. When wind speeds exceed 4 m s^{-1}, the dispersion effect is significantly enhanced, and concentrations decrease noticeably. In addition, the diurnal characteristics of industrial production also indirectly affect concentration fluctuations, further increasing the frequency of high concentration episodes.

3.2 Evaluation of WRF Simulation Results

The WRF-GHG simulation results were compared and validated against Lidar detection data and sensor-collected data, as shown in Table 2. Figure 3d presents a comparison between the WRF simulated CO_2 concentrations and the Lidar measurements at the park's emission source. While the two datasets exhibit good consistency in temporal variability, substantial discrepancies remain in their absolute values. The CO_2 concentration simulated by WRF-GHG ranges from 420 to 460 ppm, while the Lidar-measured CO_2 concentration ranges from 450 to 800 ppm. This is associated with the emission inventory adopted by WRF and the unique terrain of the park's location. The EDGAR_2024_GHG dataset used in the simulation has a latitudinal and longitudinal resolution of only 0.1° and a temporal resolution of monthly data. These resolutions are insufficiently detailed for such specific park emissions. Additionally, the northern Luoyuan Bay where the park is situated is surrounded by mountains on three sides and adjacent to the sea on one side; this unique terrain poses a significant challenge for the terrain data inherently used by WRF.

Figure 3a–c shows the comparisons between the WRF simulation results and the data from the 2m temperature, humidity, and pressure sensors placed near the Lidar. The correlation coefficient (R) between simulated and measured air temperature is 0.96, 0.84 for relative humidity, and 0.99 for atmospheric pressure. This indicates that the WRF simulation performs well in terms of temperature, humidity, and atmospheric pressure. Figure 3d-f presents the comparisons between the WRF simulation results, and the synchronous horizontal wind speed and direction detected by the CO_2 Lidar at the emission source. Among these, the correlation coefficient (R) for 10m wind speed is 0.7 with RMSE of 1.45 m s^{-1}, indicating that WRF underestimates wind speed to a certain extent; the RMSE for 10m wind direction is 74.35°.

Table 2 Statistical evaluation of WRF-GHG simulation results. The mean bias error (MBE), root-mean-square error (RMSE), and Pearson correlation coefficient (CORR) are used to assess the performance of the WRF-GHG model. Due to the significant numerical discrepancy between the simulated CO_2 results and the measured data, CO_2 is not included in the evaluation.

Variable	MB	RMSE	R
Wind speed	-0.15	1.45	0.70
Wind direction	-	74.35	-
Temperature	-0.52	1.68	0.96
Relative Humidity	-5.59	12.63	0.84
Pressure	0.6	0.97	0.99

https://doi.org/10.5194/egusphere-2025-6470
Preprint. Discussion started: 25 February 2026

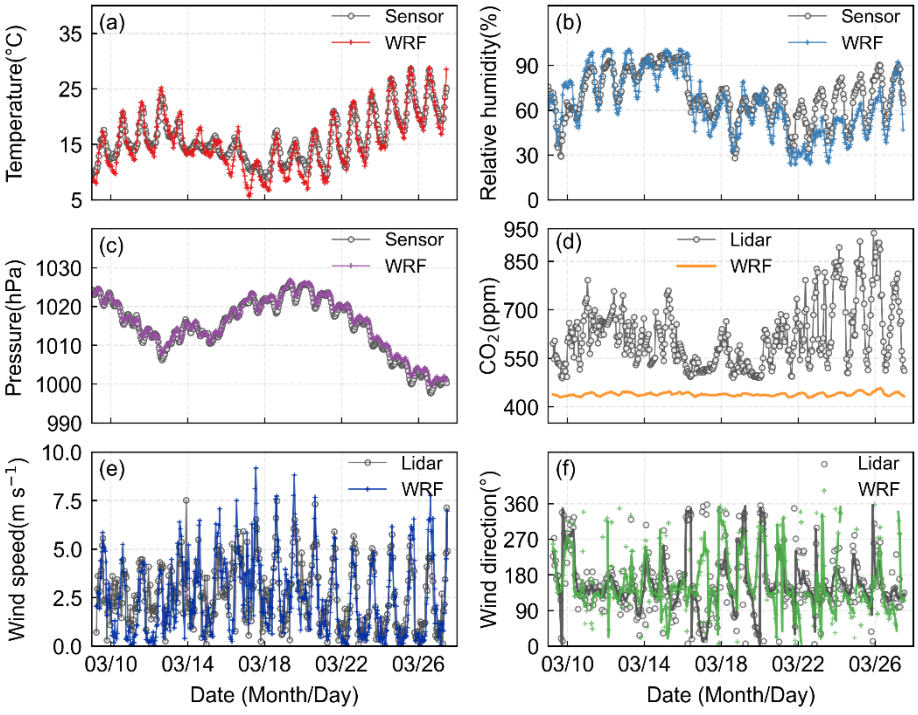

Figure 3. Comparison between WRF simulation results and observational data: (a-c) Comparison of WRF simulation results with data from temperature, humidity, and pressure sensors deployed within the industrial park; (d) Comparison of CO_2 concentrations at the industrial park's emission source from WRF simulations and CO_2 Lidar measurements; (e-f) Comparison of wind field data at the emission source from WRF simulations and synchronous CO_2 Lidar observations.

3.3 CO_2 spatiotemporal analysis using Lidar and WRF simulations

Based on the distribution of average CO_2 concentrations during the study period, 24–26 March (the period with the highest concentrations) was selected for in-depth analysis. The comparison of CO_2 Lidar observations with WRF simulation results in these three days are shown in Fig. 4-6.

Figure 4 presents partial observation results of the Lidar and synchronous WRF simulation data from 06:00 to 00:00 LT on 24 March. As shown in the Lidar observations (Figure 4a-h), the CO_2 dispersion characteristics at different time periods were highly correlated with wind field conditions. At 06:31 LT, the entire industrial park was under calm wind conditions. Emitted CO_2 accumulated within the 0–1.5 km radial range of the park covered by the Lidar scan, with CO_2 concentrations stably maintained at approximately 850 ppm. In contrast, the CO_2 concentration in the far-field mountainous area (2–3 km away) — corresponding to an altitude of 300–500 m — was only about 450 ppm. At 09:09 LT, the far-field wind shifted to westerly (wind speed: 2–4 m s^{-1}), and the CO_2 accumulated in the near-field began to disperse. CO_2 at an azimuth of 16° and radial distance of 2 km was transported northeastward with the southwesterly wind. By 11:05 LT, near-surface turbulence intensified, and the wind direction in the park turned southeasterly (wind speed: 2–4 m s^{-1}), reducing the regional CO_2 concentration to

https://doi.org/10.5194/egusphere-2025-6470
Preprint. Discussion started: 25 February 2026

600 ppm. At this time, two industrial emission sources located at 1 km radial distance with 330°–340° azimuth, and 1.2 km radial distance with 10°–16° azimuth showed a concentration of 650 ppm. Affected by the dispersed CO_2 from the park, the far-field CO_2 concentration increased to around 500 ppm.

From 12:57 to 15:49 LT, the sea breeze was strong, and the park maintained a southeasterly wind (wind speed: 4–6 m s^{-1}). The high concentration of CO_2 accumulated at night had completely dispersed, with the overall CO_2 concentration in the park remaining at approximately 450 ppm. Only low-intensity emissions were detected at the sources, and CO_2 was transported from the southeast to the northwest. At 18:37 LT, the sea breeze weakened, and the wind field in the park became turbulent (wind speed: 2–4 m s^{-1}). The emission intensity increased at the source located at 1 km radial distance with 330°–350° azimuth, with CO_2 concentration reaching around 750 ppm and dispersing to the far field. In contrast, the area 2–3 km away (0°–16° azimuth) was not affected as it was not in the downwind direction of the emission source, maintaining a concentration of approximately 450 ppm.

At 20:24 LT, the near-surface wind field within 0–1 km radial distance returned to calm, and CO_2 began to reaccumulate. Influenced by the southwesterly wind, CO_2 from the park dispersed to the area 2–3 km away (350°–16° azimuth), increasing the concentration there from 450 ppm (at 18:37 LT) to approximately 600 ppm. By 23:54 LT, the wind direction in the 2–3 km radial range (corresponding to 300–500 m altitude) shifted to southwest land breeze. Combined with mountain obstruction and a decrease in Boundary Layer Height (BLH), the wind field within 0–1.5 km radial distance remained calm, hindering the outward dispersion of CO_2 from the emission sources. Consequently, the CO_2 previously dispersed to the 2–3 km range was rapidly transported northeastward by the southwesterly wind, reducing the CO_2 concentration there to below 450 ppm.

Figure 4i-p shows the WRF-simulated surface CO_2 concentrations and wind fields in Luoyuan Bay. Its variation trend is consistent with the Lidar observations: during 07:00–09:00 LT, the wind field was calm, CO_2 accumulated in the bay, and the simulated concentration in the park was approximately 445 ppm. From 11:00 to 16:00 LT, the park was dominated by southeasterly winds (wind speed: 2–6 m s^{-1}), with relatively low overall CO_2 concentrations. From 19:00 to 00:00 on 25 March, the near-surface wind field returned to calm, and the CO_2 concentration gradually increased.

Figure 5 presents a comparison between the CO_2 Lidar observation data and the WRF numerical simulation results with corresponding timestamps on 25 March 2025. As can be seen from the figure, the Lidar successfully captured the significant dynamic changes in CO_2 concentrations within the industrial park.

Based on the Lidar observation data (Fig. 5a-h), the wind field within the park remained generally calm from 01:34 to 04:11 local time. CO_2 emissions continuously accumulated within the range of 0 to 1.8 km from the Lidar (equivalent to an altitude of approximately 300 m above the ground), with concentrations exceeding 700 ppm and an average value of around 800 ppm. At 08:32 LT, the near-field wind was calm, and the CO_2 concentration reached a peak. Subsequently, with the onset of northwest winds in the far-field, the high concentration of CO_2 plume dispersed outward by approximately 2.5 km, covering most of the industrial park and parts of the mountainous areas.

https://doi.org/10.5194/egusphere-2025-6470
Preprint. Discussion started: 25 February 2026

From 13:23 to 15:13 LT, the southeasterly wind speed within the park reached 2 to 4 m s^{-1}. During this period, the previously accumulated CO_2 was dispersed and transported, resulting in a significant decrease in the overall park CO_2 concentration from 800 ppm to 500–550 ppm. Meanwhile, a local emission source was observed approximately 700 m from the Lidar at an azimuth of 335°, with a concentration of 650 ppm. At 16:57 LT, when the southeasterly wind speed reached 4 m s^{-1}, a distinct high concentration of CO_2 plume was observed at an azimuth of 310°–350° and a radial distance of 500 m, with a concentration of 650 ppm. This plume dispersed extensively from the southeast to the northwest. From 21:20 to 23:06 LT, the wind field became calm again. CO_2 emissions reaccumulated, forming a high concentration zone (>700 ppm) within the range of 0 to 2 km, while the far-field concentration remained at a relatively low level of approximately 450 ppm.

Figure 5i-p shows the simulation results of WRF-GHG, with the location of the industrial park marked by a red asterisk in the corresponding WRF domain. From 02:00 to 08:00 LT on the 25th, the wind was very weak across the entire Luoyuan Bay area. During this period, the CO_2 concentration near the industrial park gradually increased from 450 ppm to 460 ppm. From 13:00 to 17:00 LT, due to the combined effects of enhanced sea breezes and plant photosynthesis, the CO_2 concentration across the entire bay remained at a low level. However, from 21:00 to 23:00 LT, as the wind field in the bay became calm again, the CO_2 concentration in the industrial park began to rise.

Figure 6 presents the Lidar observation results and WRF surface simulation data of 26 March, with the CO_2 transport and dispersion closely associated with the diurnal variation of wind fields. At 02:37 LT, the wind direction was southeasterly within the 1–1.5 km radial range (corresponding to 150–250 m altitude) and southerly within the 1.5–3 km radial range (corresponding to 250–500 m altitude), promoting the transport of CO_2 accumulated from industrial emissions to the far field. By 05:16 LT, the calm wind area expanded to the 2 km radial range, and a high concentration zone of nearly 900 ppm was formed within the 0–1.8 km range. At 06:09 LT, CO_2 emitted from the park continued to accumulate in the valley and spread outward; the wind plume detected at 1.2 km radial distance and 345° azimuth was the resultant vector of the emission source plume velocity (observed by Lidar) and the weak wind field in the park. From 08:48 to 10:32 LT, post-sunrise turbulence intensified, and the park was dominated by a southeasterly wind with a speed of 2–4 m s^{-1}. CO_2 dispersed throughout the Lidar scanning range, with concentrations maintained at 550–650 ppm. During 12:17–17:41 LT, the sea breeze was strong (4–6 m s^{-1}), and distinct CO_2 plumes from emission sources were clearly identified. Correspondingly, the WRF simulation results (Fig. 6i–k) indicate that the entire Luoyuan Bay was in a relatively high CO_2 concentration state. The CO_2 concentration increased gradually from 03:00 to 06:00 LT and peaked at 06:00 LT. Subsequently, the CO_2 concentration in the park decreased gradually (Fig. 6l–p), which is consistent with the variation trend of Lidar observations. Joint analysis of the high concentration period (24–26 March) reveals that both the Lidar and WRF model captured the core dynamic of CO_2: "nighttime accumulation and daytime dispersion". The dispersion and accumulation processes are jointly influenced by wind fields (sea-land breeze transition, wind speed) and terrain (mountain obstruction). The Lidar accurately identifies local emission plumes and small-scale dispersion details, while the model reproduces the overall regional variation trend. These two approaches complement each other to verify the complex dispersion mechanism of CO_2 in the semi-enclosed bay.

https://doi.org/10.5194/egusphere-2025-6470
Preprint. Discussion started: 25 February 2026

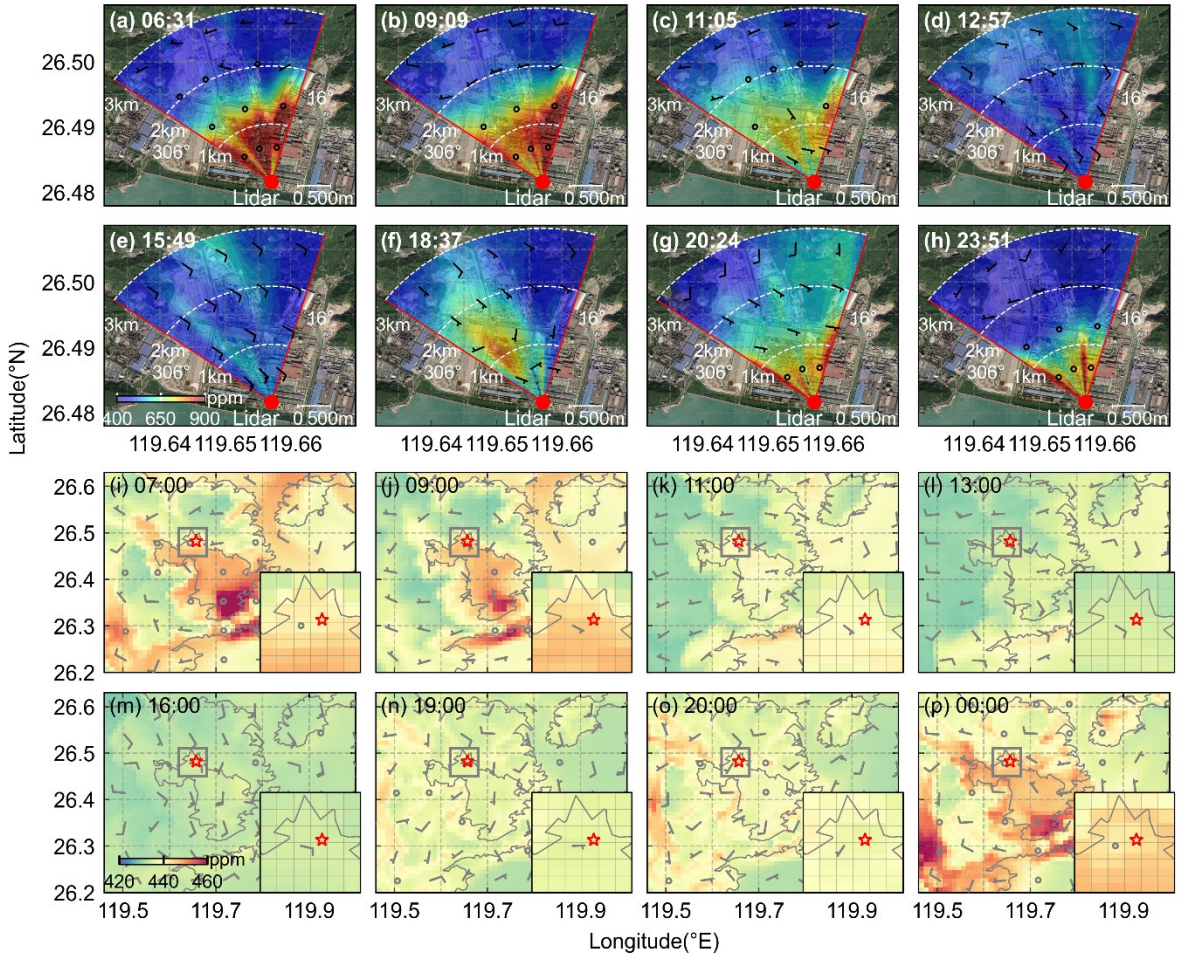

Figure 4. Partial detection results of the CO_2 Lidar and simulation results of WRF-GHG at corresponding times on 24 March 2025 (LT; UTC+8); (a)–(h) are the CO_2 Lidar observation results; (i)–(p) are the WRF-GHG simulation results in the surface layer, with the magnified location of the industrial park shown in the bottom right corner. Wind speed is uniformly represented by short dashes and small triangles perpendicular to the right side of the end of the wind direction bar (in the Northern Hemisphere), where long dashes represent 4 m s^{-1}, short dashes represent 2 m s^{-1}, triangles represent 20 m s^{-1}, and wind speeds less than 2 m s^{-1} are represented as open circles. Map source: Microsoft Bing Maps 2026.

https://doi.org/10.5194/egusphere-2025-6470
Preprint. Discussion started: 25 February 2026

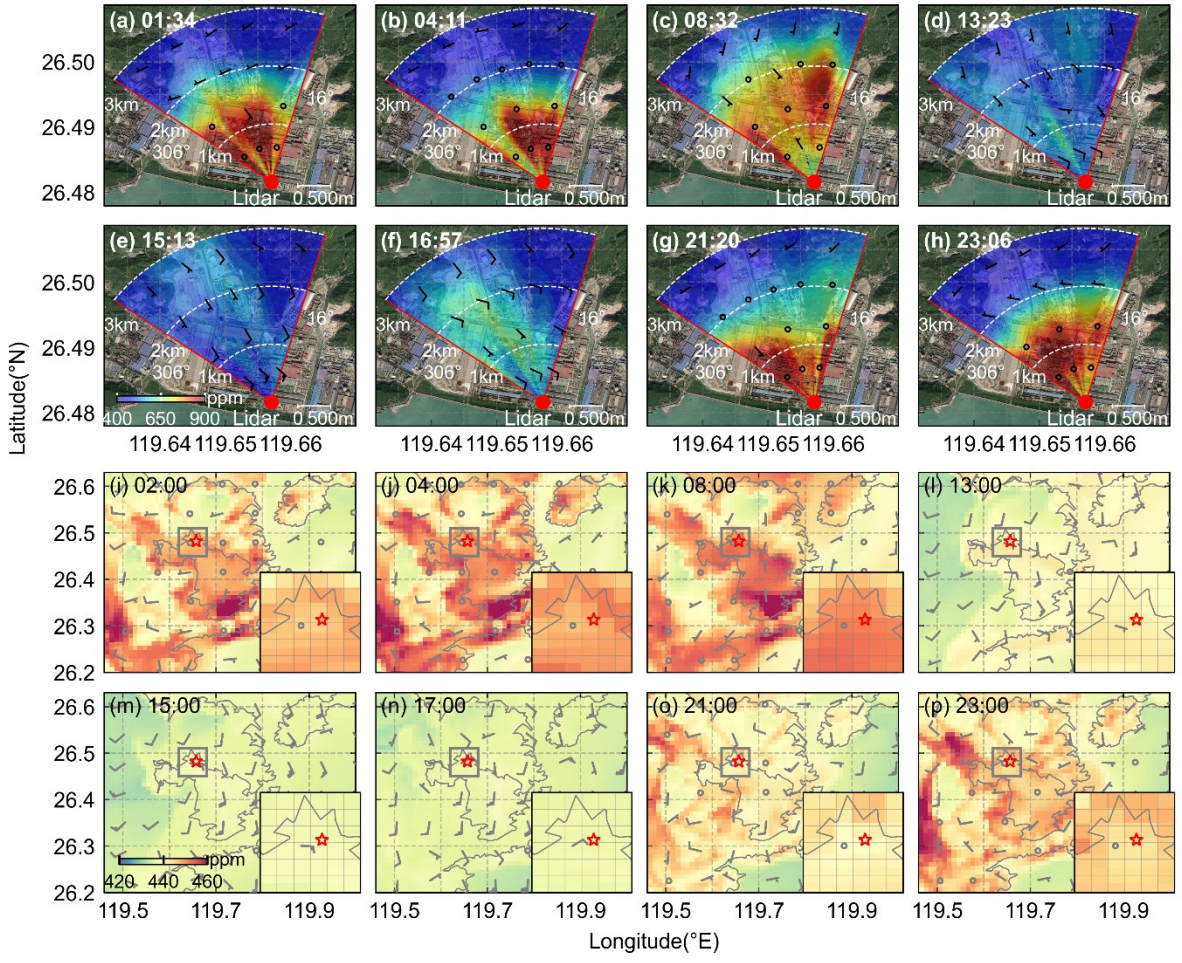

Figure 5. Partial detection results of the CO_2 Lidar and simulation results of WRF-GHG at corresponding times on 25 March 2025 (LT; UTC+8); (a)–(h) are the CO_2 Lidar observation results; (i)–(p) are the WRF-GHG simulation results in the surface layer, with the magnified location of the industrial park shown in the bottom right corner. Wind speed is uniformly represented by short dashes and small triangles perpendicular to the right side of the end of the wind direction bar (in the Northern Hemisphere), where long dashes represent 4 m s^{-1}, short dashes represent 2 m s^{-1}, triangles represent 20 m s^{-1}, and wind speeds less than 2 m s^{-1} are represented as open circles. Map source: Microsoft Bing Maps 2026.

https://doi.org/10.5194/egusphere-2025-6470
Preprint. Discussion started: 25 February 2026

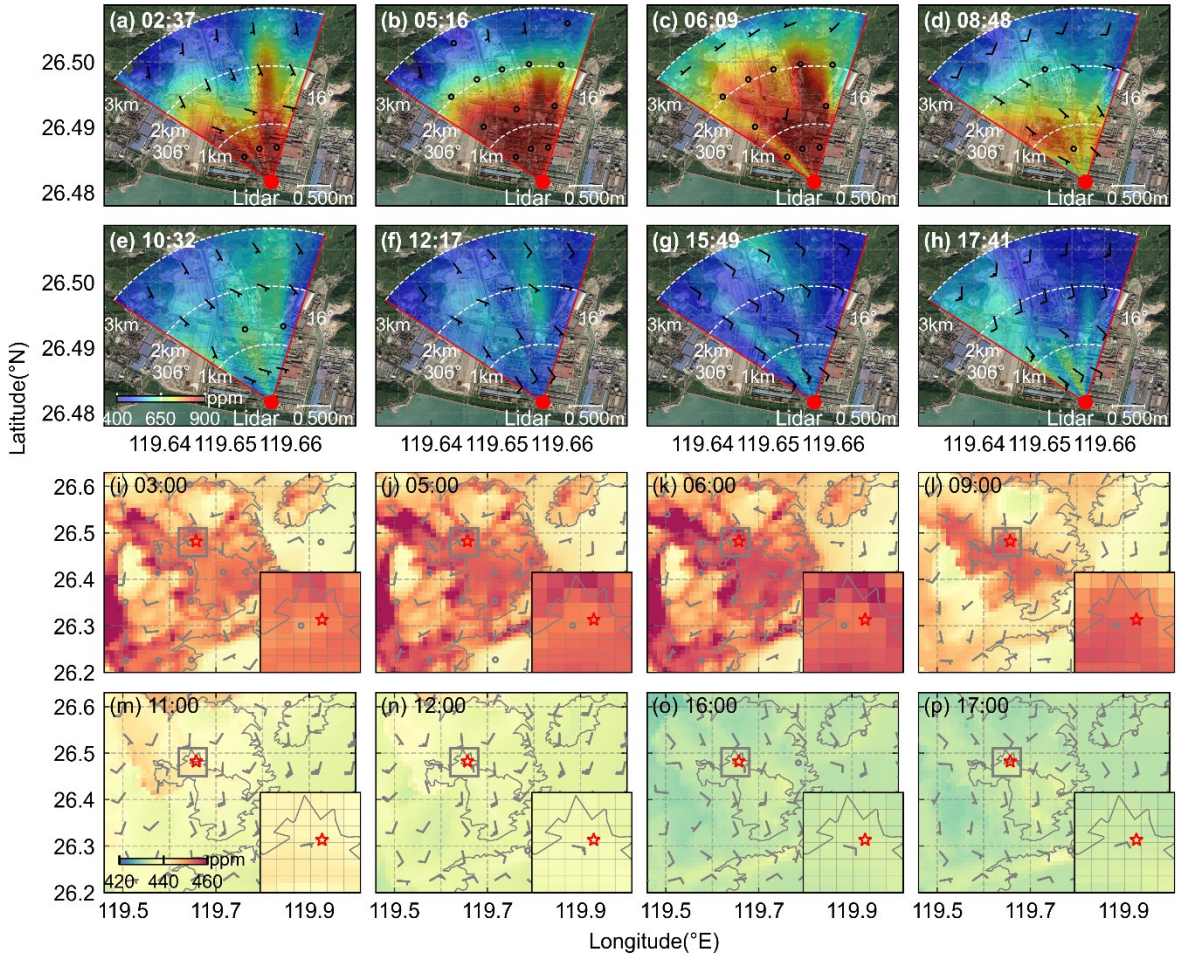

Figure 6. Partial detection results of the CO_2 Lidar and simulation results of WRF-GHG at corresponding times on 26 March 2025 (LT; UTC+8); (a)–(h) are the CO_2 Lidar observation results; (i)–(p) are the WRF-GHG simulation results in the surface layer, with the magnified location of the industrial park shown in the bottom right corner. Wind speed is uniformly represented by short dashes and small triangles perpendicular to the right side of the end of the wind direction bar (in the Northern Hemisphere), where long dashes represent 4 m s^{-1}, short dashes represent 2 m s^{-1}, triangles represent 20 m s^{-1}, and wind speeds less than 2 m s^{-1} are represented as open circles. Map source: Microsoft Bing Maps 2026.

https://doi.org/10.5194/egusphere-2025-6470
Preprint. Discussion started: 25 February 2026

3.4 Vertical CO_2 accumulation and dispersion

Figure 7a shows the results of Lidar's 10° elevation angle scanning converted to vertical height. The portion above 500 m (white dashed line) is considered invalid data. Figure 7b shows the WRF-simulated CO_2 concentrations at the park location, with the black solid line representing the model-output BLH. Figure 7c–e represents the model-output vertical wind speed, horizontal wind speed, and horizontal wind direction, respectively. Figure 7f presents the model-output air temperature, with the black dashed line indicating the strongest temperature inversion layer where the temperature gradient exceeds 0.5 °C 100 m^{-1}.

Although there is a significant numerical discrepancy between the observed and simulated results, their trends are highly consistent. Atmospheric BLH and atmospheric stability are the two primary factors controlling the vertical distribution of CO_2 (Li et al., 2014). The BLH decreases at night, approaching the surface, and the inversion layer can reach a thickness of 200 m, inhibiting the upward dispersion of CO_2. By creating a stable atmospheric stratification and weakening turbulence, the inversion layer effectively impedes the vertical mixing of momentum, heat, and pollutants; meanwhile, it restricts vertical and horizontal dispersion processes, trapping pollutants within the inversion layer (Li et al., 2021; Zong et al., 2023; Sun et al., 2025).

Additionally, due to the calm wind conditions in the park and its location in a low-lying valley surrounded by mountains on three sides and adjacent to the sea to the south, the horizontal dispersion of emitted CO_2 is hindered, leading to local accumulation of CO_2 and the formation of high concentration zones. After sunrise during the daytime, near-surface turbulence intensifies, horizontal wind speed increases, upward vertical wind strengthens, and the BLH rises. Consequently, the CO_2 accumulated at night begins to transport and disperse, resulting in a decrease in CO_2 concentrations within the park.

Vertical cross-sections of the WRF-Chem simulation results on 25 March 2025 were plotted along the line from (26.65°N, 119.65°E) to (26.18°N, 119.67°E), yielding the vertical distributions of CO_2 concentrations and wind fields (Fig. 8). The shaded area represents terrain elevation, and the park is located at (26.47°N, 119.65°E). Luoyuan Bay lies between two mountains, and the impact of mountainous terrain on the wind field within the bay is mainly concentrated below 500 m. Due to the terrain, winds are blocked by the surrounding high mountains, resulting in changes in wind direction within the bay and wind speeds significantly lower than those in the coastal areas outside the bay. This is not conducive to pollutant dispersion and dilution. From 02:00 to 08:00 LT on 25 March, the lower atmosphere in Luoyuan Bay was stable, with near-calm conditions in the park. CO_2 accumulated within the bay, mainly concentrated below 500 m above sea level, with simulated concentrations exceeding 450 ppm. From 13:00 to 17:00 LT, turbulence intensified and the wind field in Luoyuan Bay strengthened. The CO_2 accumulated at night began to disperse; driven by upward vertical winds, it crossed the high mountains and dispersed into the upper atmosphere. Local circulations formed near the high mountains, transporting CO_2 from the lower layers to the upper layers. From 21:00 to 23:00 LT, the atmospheric environment in the bay returned to a stable state. CO_2 emitted by the industrial park in the bay accumulated again in the coastal boundary layer below 500 m above sea level, leading to prolonged pollutant residence time and enhanced CO_2 concentration accumulation effect within the bay.

https://doi.org/10.5194/egusphere-2025-6470
Preprint. Discussion started: 25 February 2026

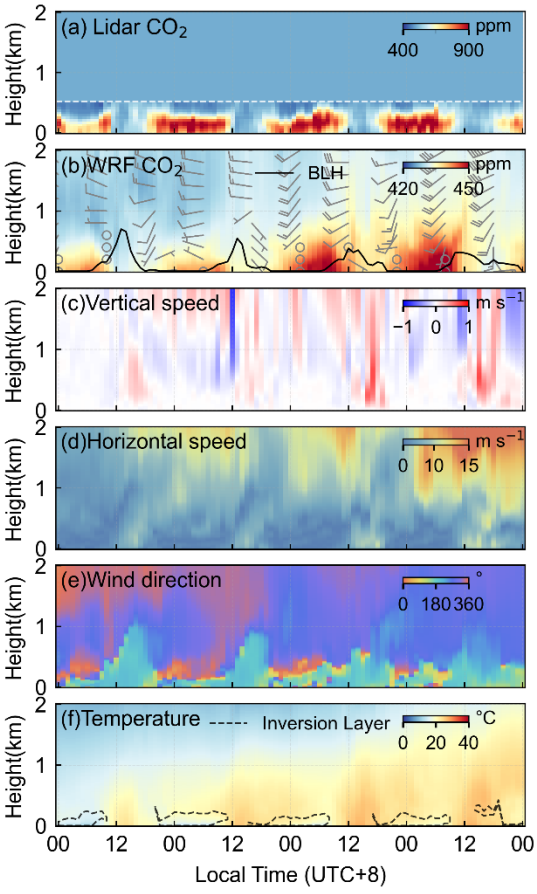

Figure 7. Time-series heatmaps of CO_2 Lidar observations and WRF simulation results from 00:00 local time (LT; UTC+8) on 23 March to 00:00 LT on 27 March 2025; (a) shows the distribution results of CO_2 detected by the CO_2 Lidar converted to vertical height, where the portion above 500 m (white dashed line) is invalid data; (b) presents the WRF-simulated CO_2 concentrations at the park location, with the black solid line representing the model-output BLH; (c)–(e) are the model-output vertical wind speed, horizontal wind speed, and horizontal wind direction, respectively; (f) is the model-output air temperature, where the black dashed line denotes the strongest temperature inversion layer with a temperature gradient exceeding 0.5 °C 100 m^{-1}.

https://doi.org/10.5194/egusphere-2025-6470
Preprint. Discussion started: 25 February 2026

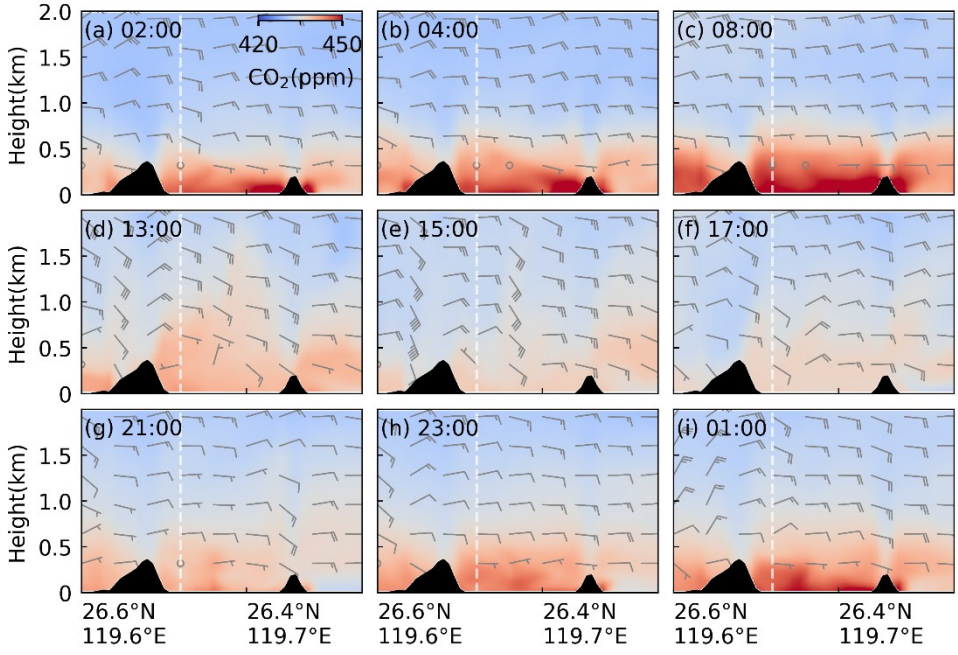

Figure 8. Vertical distributions of CO_2 concentrations and wind fields along the cross-section from (26.65°N, 119.65°E) to (26.18°N, 119.67°E) based on WRF simulation results on 25 March 2025 (LT; UTC+8); shaded areas represent mountainous terrain; the white dashed line denotes the location of the studied industrial park.

4. Discussion and Conclusion

This study comprehensively analysed the accumulation, dispersion characteristics, and driving mechanisms of CO_2 in an industrial park under the terrain of the semi-enclosed Luoyuan Bay, based on Lidar observations and WRF-GHG model simulations. The Lidar observation results revealed obvious diurnal variations and spatial distribution differences in the park's CO_2 concentrations, a feature closely related to Luoyuan Bay's terrain (surrounded by mountains on three sides and adjacent to the sea on one side) and the diurnal transition of sea-land breeze circulation. This observation framework not only achieves accurate quantification of CO_2 dynamics but also establishes a new observational paradigm for capturing small-scale, terrain-regulated carbon transport processes, filling the critical gap between coarse satellite remote sensing and sparse in-situ measurements in complex coastal-industrial environments. At night (Fig. 9a), under the combined influence of calm wind fields, temperature inversion layers, and valley terrain, CO_2 continuously accumulates in low-lying areas, with concentrations exceeding 700 ppm and reaching a maximum of 940 ppm. During the daytime (Fig. 9b), driven by the enhanced southeasterly sea breezes originating from the East China Sea, intensified near-surface turbulence, and BLH rise, CO_2 is diluted through horizontal transport toward the northwest downwind direction and vertical dispersion over the high mountain terrain, with concentrations significantly decreasing to 500–550 ppm. CO_2 concentration is significantly negatively correlated with wind

https://doi.org/10.5194/egusphere-2025-6470
Preprint. Discussion started: 25 February 2026

speed; low wind speed combined with terrain obstruction constitutes a key inducement for pollutant retention and accumulation. Although sea breezes can promote dispersion, the hindering effect of mountain terrain weakens their horizontal penetration, resulting in a slower CO_2 dilution rate in the bay compared to open coastal areas. Naturally, the contribution of transboundary transport to local high concentrations cannot be neglected (Daellenbach et al., 2024).

The WRF-GHG model showed good consistency with the Lidar observations in simulating the diurnal variation trend of CO_2 concentrations, but the simulated values (420–460 ppm) were systematically lower than the Lidar observations (450–900 ppm). The root cause of this numerical deviation is closely related to the complex terrain of the bay, the accuracy of the emission inventory, and insufficient wind field simulation. Firstly, the EDGAR emission inventory adopted by the model has a spatial resolution of only 0.1° and a temporal resolution of monthly scale, making it difficult to accurately characterize the high-intensity, hourly-scale dynamic industrial emission characteristics of the park. Furthermore, the existing boundary layer parameterization scheme of the model fails to fully consider the terrain-following effect of the semi-enclosed bay and the refined process of sea-land breeze transition, leading to inadequate simulation of the process where the temperature inversion layer and mountain terrain synergistically inhibit vertical dispersion, and ultimately resulting in a systematic deviation in CO_2 concentration simulation.

Notably, the interaction between the topographic characteristics of the semi-enclosed Luoyuan Bay and sea breeze circulation forms a unique CO_2 dispersion mechanism distinct from that of open coastal or plain areas. Mountain terrain not only directly hinders the wind field but also forms secondary circulations by altering the local pressure field, resulting in CO_2 being hindered in both horizontal and vertical dispersion under the dual inhibition of "terrain-temperature inversion layer". Even with enhanced sea breezes during the daytime, CO_2 concentrations in the bay remain higher than those in open areas. This phenomenon confirms the "buffering effect" of terrain on high concentration CO_2 from industrial emissions cannot readily be transported out of the enclosed bay and can only achieve partial dilution through vertical uplift. At night, under the combined action of land breezes, stable stratification, and terrain, CO_2 is confined to the near-surface layer, forming a cycle of "nighttime accumulation-daytime dispersion" and extending the residence time of pollutants in the bay. Meanwhile, the high spatiotemporal resolution of the Lidar accurately captures the terrain-driven small-scale CO_2 plume migration, verifying the superiority of Lidar technology in monitoring industrial emissions under complex terrain and providing high-precision data support for the attribution analysis of model deviations.

This study demonstrates the advantages of Lidar in monitoring industrial CO_2 emissions with high spatiotemporal resolution and highlights the limitations of the WRF-GHG model in characterizing complex terrain and refined emission sources. The CO_2 Lidar fills the critical observational gap in small-scale, terrain-regulated carbon transport processes in complex coastal-industrial environments. It also provides an empirical basis for validating and optimising the parameterisation schemes of carbon cycle processes in regional climate models. Future research could focus on three key areas: (1) Optimizing the model and upgrading data: replacing the EDGAR dataset with localized industrial emission statistics at hourly temporal resolution. Plant-level emission point source data should be incorporated to improve spatial accuracy. High-resolution topographic datasets will be implemented for the WRF model. Additionally, boundary layer parameterization schemes require refinement

https://doi.org/10.5194/egusphere-2025-6470
Preprint. Discussion started: 25 February 2026

to enhance simulation accuracy of bay topography and sea breeze interactions. (2) Promoting multi-source data fusion and assimilation: integrating Lidar observations, satellite XCO_2 data, and ground sensor networks to construct a multi-source data assimilation system and incorporating high spatiotemporal resolution observation data into the model to reduce systematic deviations. (3) Conducting long-term observations and deepening mechanism research: exploring how variations in sea breeze intensity and direction affect CO_2 dispersion through cross-seasonal observations; focusing on the coupling mechanism between local circulation and carbon emissions in semi-enclosed bays; and developing targeted emission dispersion assessment models. These efforts will provide a more scientific theoretical basis and technical support for total carbon emission control, pollution emergency plan formulation, and regional environmental governance of bay-type industrial parks. This study provides a typical case for the observation and simulation of carbon emissions under special terrain. In the future, the deep integration of Lidar observations with the model will contribute to reducing uncertainties in regional carbon emission accounting. Furthermore, it is expected to improve the precise management and control capabilities of regional carbon emissions, and ultimately contribute to reducing uncertainties in global carbon cycle assessments and enhancing the reliability of climate change mitigation strategies.

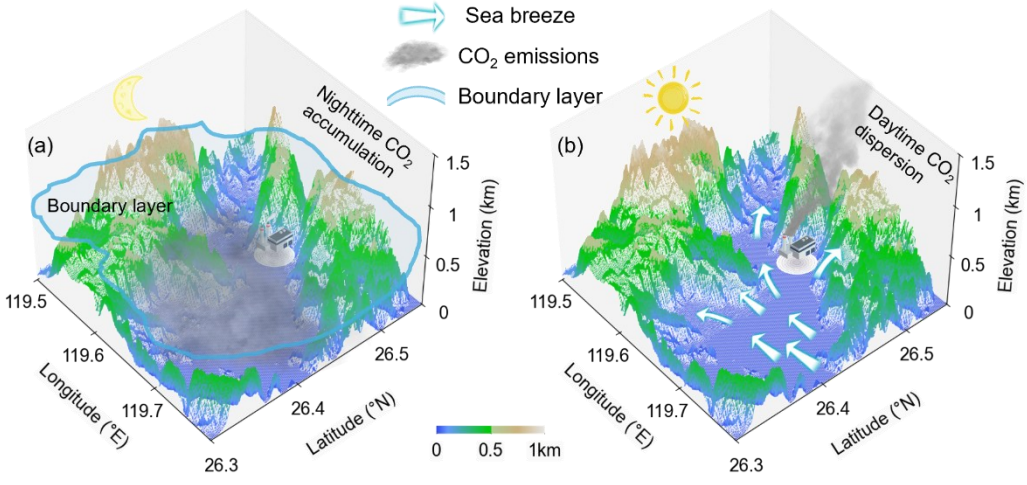

Figure 9. Schematic diagram of the impact of semi-enclosed bay terrain on CO_2 dispersion and transport; (a) At night, CO_2 emitted from the Luoyuan Bay industrial park accumulates inside the bay under the synergistic effect of calm wind fields, temperature inversion layers and valley terrain; (b) During the day, the strengthened sea breeze enters the bay from the southeast, and the CO_2 emitted from the industrial park diffuses and transports toward the northwest.

https://doi.org/10.5194/egusphere-2025-6470
Preprint. Discussion started: 25 February 2026

Code and Data Availability.

The data required to run the WRF-GHG model are publicly available from the ERA5 dataset at https://doi.org/10.24381/cds.adbb2d47 (Hersbach et al., 2023a, last access: 1 December 2025) and https://doi.org/10.24381/cds.bd0915c6 (Hersbach et al., 2023b, last access: 1 December 2025), the CAMS dataset at https://doi.org/10.24381/93910310 (Agustí-Panareda et al., 2022, last access: 1 December 2025) which provides CO_2 initial and boundary conditions, EDGAR_2024_GHG at https://publications.jrc.ec.europa.eu/repository/handle/JRC138862 (Crippa et al., 2024, last access: 1 December 2025) for anthropogenic emissions, CLMS data at https://doi.org/10.2909/c6377c6e-76cc-4d03-8330-628a03693042 (last access: 1 December 2025), and the JMA Ocean CO_2 Map dataset at https://www.data.jma.go.jp/kaiyou/english/co2_flux/co2_flux_data_en.html (Iida et al., 2021, last access: 1 December 2025) for oceanic CO_2 flux data; the code for modifying WRF initial and boundary conditions is available at https://github.com/rnoeliab/WRF-GHG-Prepy (provided by Benavente, Noelia Rojas, last access: 1 December 2025). All relevant codes and data of this study can be obtained by contacting the corresponding author.

Author contributions.

DY was responsible for data collection and collation, model simulation, data analysis, and drafted the manuscript; QX participated in data collection and collation, data analysis, assisted in model establishment, and provided professional knowledge and guidance on Lidar data processing; SY and YC engaged in data collection and collation and offered professional expertise in Lidar data processing and analysis; KX, HH, JG, KG and JH provided professional guidance on data processing and analysis; ZZ, JC, YY, and HX offered guidance and support during data analysis and manuscript writing, revised and edited the manuscript. ZZ and XY Supervised the project. All authors provided critical feedback that helped shape the research, analysis, and final version of the paper.

Competing Interests.

The authors declare that they have no known competing financial interests or personal relationships that could have appeared to influence the work reported in this paper.

Disclaimer.

Publisher's note: Copernicus Publications remains neutral with regard to jurisdictional claims made in the text, published maps, institutional affiliations, or any other geographical representation in this paper. The authors bear the ultimate responsibility for providing appropriate place names. Views expressed in the text are those of the authors and do not necessarily reflect the views of the publisher.

https://doi.org/10.5194/egusphere-2025-6470
Preprint. Discussion started: 25 February 2026

Acknowledgments.

We are grateful to Benavente, Noelia Rojas for sharing the code for modifying WRF initial and boundary conditions at https://github.com/rnoeliab/WRF-GHG-Prepy (last access: 1 December 2025). We also appreciate Callewaert, S. for providing the tutorial on WRF-GHG at https://doi.org/10.18758/Q6RAPNEU (last access: 1 December 2025). Additionally, we thank Bing Maps for providing remote sensing map services.

Financial Support.

This work was supported by the National Natural Science Foundation of China (Nos. 42305147 and 42405138), the Natural Science Foundation of Jiangsu Province (No. BK20230428) and the National Key Research and Development Program of China (2022YFF0606400).

References

Agustí-Panareda, A., McNorton, J., Balsamo, G., Baier, B. C., Bousserez, N., Boussetta, S., Brunner, D., Chevallier, F., Choulga, M., Diamantakis, M., Engelen, R., Flemming, J., Granier, C., Guevara, M., Denier Van Der Gon, H., Elguindi, N., Haussaire, J.-M., Jung, M., Janssens-Maenhout, G., Kivi, R., Massart, S., Papale, D., Parrington, M., Razinger, M., Sweeney, C., Vermeulen, A., and Walther, S.: Global nature run data with realistic high-resolution carbon weather for the year of the paris agreement, Sci. Data, 9, 160–173, https://doi.org/10.1038/s41597-022-01228-2, 2022.

Ahmadov, R., Gerbig, C., Kretschmer, R., Koerner, S., Neininger, B., Dolman, A. J., and Sarrat, C.: Mesoscale covariance of transport and CO_2 fluxes: Evidence from observations and simulations using the WRF-VPRM coupled atmosphere-biosphere model, J. Geophys. Res.: Atmos., 112, 2007JD008552, https://doi.org/10.1029/2007JD008552, 2007.

Alberti, R. C. A., Lauvaux, T., Vara-Vela, A. L., Barrero, R. S., Karoff, C., Andrade, M. D. F., Marques, M. T. A., Benavente, N. R., Cabral, O. M. R., Da Rocha, H. R., and Ynoue, R. Y.: Monitoring and modeling seasonally varying anthropogenic and biogenic CO_2 over a large tropical metropolitan area, https://doi.org/10.5194/egusphere-2024-3060, 24 October 2024.

Beck, V., Gerbig, C., Koch, T., Bela, M. M., Longo, K. M., Freitas, S. R., Kaplan, J. O., Prigent, C., Bergamaschi, P., and Heimann, M.: WRF-chem simulations in the amazon region during wet and dry season transitions: Evaluation of methane models and wetland inundation maps, Atmos. Chem. Phys., 13, 7961–7982, https://doi.org/10.5194/acp-13-7961-2013, 2013.

Bisht, J. S. H., Patra, P. K., Takigawa, M., Kanaya, Y., Yamaguchi, M., Machida, T., and Tanimoto, H.: CO2 high-resolution simulation using WRF-GHG over the kanto region in Japan, https://doi.org/10.22541/essoar.168626399.94131688/v1, 8 June 2023.

Bisht, J. S. H., Patra, P. K., Takigawa, M., Kanaya, Y., Yamaguchi, M., Machida, T., and Tanimoto, H.: High-Resolution Simulation of CO_2 Using WRF-GHG Over the Kanto Region in Japan, J. Geophys. Res.: Atmos., 130, e2025JD043589, https://doi.org/10.1029/2025JD043589, 2025.

Callewaert, S., Zhou, M., Langerock, B., Wang, P., Wang, T., Mahieu, E., and De Mazière, M.: A WRF-chem study of the greenhouse gas column and in situ surface concentrations observed at xianghe, china. Part 1: methane (CH_4), https://doi.org/10.5194/egusphere-2024-3228, 29 October 2024.

https://doi.org/10.5194/egusphere-2025-6470
Preprint. Discussion started: 25 February 2026

Callewaert, S., Zhou, M., Langerock, B., Wang, P., Wang, T., Mahieu, E., and De Mazière, M.: A WRF-chem study of the greenhouse gas column and in situ surface mole fractions observed at xianghe, China. Part 2: Sensitivity of carbon dioxide (CO_2) simulations to critical model parameters, https://doi.org/10.5194/egusphere-2025-3959, 4 September 2025.

Crippa, M., Guizzardi, D., Pagani, F., Banja, M., Muntean, M., Schaaf, E., Monforti-Ferrario, F., Becker, W. E., Quadrelli, R., Risquez Martin, A., Taghavi-Moharamli, P., Köykkä, J., Grassi, G., Rossi, S., Melo, J., Oom, D., Branco, A., San-Miguel, J., Manca, G., Pisoni, E., Vignati, E., & Pekar, F. (2024). GHG emissions of all world countries (JRC138862). Publications Office of the European Union. https://doi.org/10.2760/4002897

Daellenbach, K. R., Cai, J., Hakala, S., Dada, L., Yan, C., Du, W., Yao, L., Zheng, F., Ma, J., Ungeheuer, F., Vogel, A. L., Stolzenburg, D., Hao, Y., Liu, Y., Bianchi, F., Uzu, G., Jaffrezo, J.-L., Worsnop, D. R., Donahue, N. M., and Kulmala, M.: Substantial contribution of transported emissions to organic aerosol in beijing, Nat. Geosci., 17, 747–754, https://doi.org/10.1038/s41561-024-01493-3, 2024.

Deng, Z., Zhu, B., Davis, S. J., Ciais, P., Guan, D., Gong, P., and Liu, Z.: Global carbon emissions and decarbonization in 2024, Nat. Rev. Earth Environ., 6, 231–233, https://doi.org/10.1038/s43017-025-00658-x, 2025.

Dong, X., Yue, M., Jiang, Y., Hu, X.-M., Ma, Q., Pu, J., and Zhou, G.: Analysis of CO_2 spatio-temporal variations in China using a weather–biosphere online coupled model, Atmos. Chem. Phys., 21, 7217–7233, https://doi.org/10.5194/acp-21-7217-2021, 2021.

Fan, D., Cheng, T., Zhu, H., Ye, X., Tang, T., Tong, H., Li, X., and Zhang, L.: Pollution-carbon synergy significantly enhances the capability of tracking power plants' CO_2 emissions from space, Environ. Sci. Technol., 59, 10919–10928, https://doi.org/10.1021/acs.est.5c01100, 2025.

Glauch, T., Marshall, J., Gerbig, C., Botía, S., Gałkowski, M., Vardag, S. N., and Butz, A.: pyVPRM: a next-generation vegetation photosynthesis and respiration model for the post-MODIS era, https://doi.org/10.5194/egusphere-2024-3692, 21 January 2025.

Gurney, K. R., Law, R. M., Denning, A. S., Rayner, P. J., Baker, D., Bousquet, P., Bruhwiler, L., Chen, Y.-H., Ciais, P., Fan, S., Fung, I. Y., Gloor, M., Heimann, M., Higuchi, K., John, J., Maki, T., Maksyutov, S., Masarie, K., Peylin, P., Prather, M., Pak, B. C., Randerson, J., Sarmiento, J., Taguchi, S., Takahashi, T., and Yuen, C.-W.: Towards robust regional estimates of CO2 sources and sinks using atmospheric transport models, Nature, 415, 626–630, https://doi.org/10.1038/415626a, 2002.

Han, G., Huang, Y., Shi, T., Zhang, H., Li, S., Zhang, H., Chen, W., Liu, J., and Gong, W.: Quantifying CO2 emissions of power plants with aerosols and carbon dioxide lidar onboard DQ-1, Remote Sens. Environ., 313, 114368, https://doi.org/10.1016/j.rse.2024.114368, 2024.

Hersbach, H., Bell, B., Berrisford, P., Biavati, G., Horányi, A., Munoz Sabater, J., Nicolas, J., Peubey, C., Radu, R., Rozum, I., Schepers, D., Simmons, A., Soci, C., Dee, D., and Thépaut, J.-N.: ERA5 Hourly Data on Pressure Levels from 1940 to Present., https://doi.org/10.24381/cds.bd0915c6, 2023a.

Hersbach, H., Bell, B., Berrisford, P., Biavati, G., Horányi, A., Munoz Sabater, J., Nicolas, J., Peubey, C., Radu, R., Rozum, I., Schepers, D., Simmons, A., Soci, C., Dee, D., and Thépaut, J.-N.: ERA5 Hourly Data on Single Levels from 1940 to Present., https://doi.org/10.24381/cds.adbb2d47, 2023b.

Hu, Y., He, X., Zhou, K., Hong, Y., Zhai, X., Zhang, H., Chen, X., Wang, X., and Wen, Q.: High-resolution vertical profiling and source apportionment of CO2 using coherent differential absorption lidar in coastal urban atmosphere, Atmos. Res., 330, 108556, https://doi.org/10.1016/j.atmosres.2025.108556, 2026.

https://doi.org/10.5194/egusphere-2025-6470
Preprint. Discussion started: 25 February 2026

Iida, Y., Takatani, Y., Kojima, A., and Ishii, M.: Global trends of ocean CO2 sink and ocean acidification: An observation-based reconstruction of surface ocean inorganic carbon variables, J. Oceanogr., 77, 323–358, https://doi.org/10.1007/s10872-020-00571-5, 2021.

IPCC: Summary for Policymakers, in:ClimateChange 2023: SynthesisReport, Contribution of Working Groups I, II andIII tothe Sixth AssessmentReport of the Intergovernmental Panel on ClimateChange,edited by: Lee, H. andRomero, J., IPCC, Geneva, Switzerland,1--34,https://doi.org/10.59327/IPCC/AR6-9789291691647.001,2023.

Imasu, R., Matsunaga, T., Nakajima, M., Yoshida, Y., Shiomi, K., Morino, I., Saitoh, N., Niwa, Y., Someya, Y., Oishi, Y., Hashimoto, M., Noda, H., Hikosaka, K., Uchino, O., Maksyutov, S., Takagi, H., Ishida, H., Nakajima, T. Y., Nakajima, T., and Shi, C.: Greenhouse gases observing SATellite 2 (GOSAT-2): Mission overview, Prog. Earth Planet. Sci., 10, 33, https://doi.org/10.1186/s40645-023-00562-2, 2023.

Kaiser, J. W., Heil, A., Andreae, M. O., Benedetti, A., Chubarova, N., Jones, L., Morcrette, J.-J., Razinger, M., Schultz, M. G., Suttie, M., and Van Der Werf, G. R.: Biomass burning emissions estimated with a global fire assimilation system based on observed fire radiative power, Biogeosciences, 9, 527–554, https://doi.org/10.5194/bg-9-527-2012, 2012.

Li, Q., Zhang, H., Cai, X., Song, Y., and Zhu, T.: The impacts of the atmospheric boundary layer on regional haze in north China, npj Clim. Atmos. Sci., 4, 9, https://doi.org/10.1038/s41612-021-00165-y, 2021.

Li, Y., Deng, J., Mu, C., Xing, Z., and Du, K.: Vertical distribution of CO2 in the atmospheric boundary layer: Characteristics and impact of meteorological variables, Atmos. Environ., 91, 110–117, https://doi.org/10.1016/j.atmosenv.2014.03.067, 2014.

Lu, W., Li, X., Li, S., Cheng, T., Guo, Y., and Fang, W.: Impact of anthropogenic emission inventories on atmospheric CO2 concentrations simulated by GEOS-chem, Atmos. Res., 326, 108255, https://doi.org/10.1016/j.atmosres.2025.108255, 2025.

Queiβer, M., Granieri, D., and Burton, M.: A new frontier in CO2 flux measurements using a highly portable DIAL laser system, Sci. Rep., 6, 33834, https://doi.org/10.1038/srep33834, 2016.

Shan, C., Wang, W., Liu, C., Sun, Y., Hu, Q., Xu, X., Tian, Y., Zhang, H., Morino, I., Griffith, D. W. T., and Velazco, V. A.: Regional CO emission estimated from ground-based remote sensing at hefei site, China, Atmos. Res., 222, 25–35, https://doi.org/10.1016/j.atmosres.2019.02.005, 2019.

Shi, R., Chen, J., He, Y., Song, W., Li, D., Shu, Y., and Wang, D.: Evaluation of the performance of the latest WRF model (V4.5) in simulating surface elements and its sensitivity to the diurnal SST cycle in the south China sea, Clim. Dyn., 62, 1567–1584, https://doi.org/10.1007/s00382-023-06988-0, 2024.

Stroud, J. R., Dienstfrey, W. J., and Plusquellic, D. F.: Study on local power plant emissions using multi-frequency differential absorption LIDAR and real-time plume tracking, Remote Sens., 15, 4283, https://doi.org/10.3390/rs15174283, 2023.

Sun, M., Xie, Z., Yao, X., Wang, S., and Dong, L.: Multilayer temperature inversion structures and their potential impact on atmospheric pollution in northwest China, Atmos. Environ., 343, 120998, https://doi.org/10.1016/j.atmosenv.2024.120998, 2025.

Taylor, T. E., O'Dell, C. W., Baker, D., Bruegge, C., Chang, A., Chapsky, L., Chatterjee, A., Cheng, C., Chevallier, F., Crisp, D., Dang, L., Drouin, B., Eldering, A., Feng, L., Fisher, B., Fu, D., Gunson, M., Haemmerle, V., Keller, G. R., Kiel, M., Kuai, L., Kurosu, T., Lambert, A., Laughner, J., Lee, R., Liu, J., Mandrake, L., Marchetti, Y., McGarragh, G., Merrelli, A., Nelson, R. R., Osterman, G., Oyafuso, F., Palmer, P. I., Payne, V. H., Rosenberg, R., Somkuti, P., Spiers, G., To, C., Weir, B., Wennberg, P. O., Yu, S., and Zong, J.: Evaluating the consistency between OCO-2 and OCO-3 XCO_2 estimates derived from

https://doi.org/10.5194/egusphere-2025-6470
Preprint. Discussion started: 25 February 2026

the NASA ACOS version 10 retrieval algorithm, Atmos. Meas. Tech., 16, 3173–3209, https://doi.org/10.5194/amt-16-3173-2023, 2023.

Wang, A., Ye, X., Xu, X., Yin, X., and Xu, Y.: Settling flux and origin of particulate organic carbon in a macro-tidal semi-enclosed embayment: Luoyuan bay, southeast China coast, Estuarine Coastal Shelf Sci., 206, 38–48, https://doi.org/10.1016/j.ecss.2017.03.023, 2018.

Wang, X., Jiang, F., Wang, H., Zhang, Z., Wu, M., Wang, J., He, W., Ju, W., and Chen, J. M.: The role of OCO-3 XCO_2 retrievals in estimating global terrestrial net ecosystem exchanges, Atmos. Chem. Phys., 25, 867–880, https://doi.org/10.5194/acp-25-867-2025, 2025.

Yang, Y., Zhou, M., Langerock, B., Sha, M. K., Hermans, C., Wang, T., Ji, D., Vigouroux, C., Kumps, N., Wang, G., De Mazière, M., and Wang, P.: New ground-based fourier-transform near-infrared solar absorption measurements of XCO_2 , XCH_4 and XCO at xianghe, China, Earth Syst. Sci. Data, 12, 1679–1696, https://doi.org/10.5194/essd-12-1679-2020, 2020.

Ye, H., Shi, H., Li, C., Wang, X., Xiong, W., An, Y., Wang, Y., and Liu, L.: A coupled BRDF CO2 retrieval method for the GF-5 GMI and improvements in the correction of atmospheric scattering, Remote Sens., 14, 488, https://doi.org/10.3390/rs14030488, 2022.

Yu, S., Guo, K., Li, S., Han, H., Zhang, Z., and Xia, H.: Three-dimensional detection of CO_2 and wind using a 1.57 μm coherent differential absorption lidar, Opt. Express, 32, 21134, https://doi.org/10.1364/OE.523904, 2024.

Yu, S., Yu, D., Xia, Q., Chen, Y., Zhang, Z., and Xia, H.: Spatiotemporal characteristics of atmospheric CO2 under the influence of different industrial emission sources using lidar remote sensing in nanping, china, J. Environ. Sci., 159, 490–501, https://doi.org/10.1016/j.jes.2025.03.046, 2026.

Yuan, J., Wu, Y., Shu, Z., Su, L., Tang, D., Yang, Y., Dong, J., Yu, S., Zhang, Z., and Xia, H.: Real-time synchronous 3-D detection of air pollution and wind using a solo coherent doppler wind lidar, Remote Sens., 14, 2809, https://doi.org/10.3390/rs14122809, 2022.

Yue, B., Yu, S., Li, M., Wei, T., Yuan, J., Zhang, Z., Dong, J., Jiang, Y., Yang, Y., Gao, Z., and Xia, H.: Local-scale horizontal CO2 flux estimation incorporating differential absorption lidar and coherent doppler wind lidar, Remote Sens., 14, 5150, https://doi.org/10.3390/rs14205150, 2022.

Zhang, L., Jiang, F., He, W., Wu, M., Wang, J., Ju, W., Wang, H., Zhang, Y., Sitch, S., and Chen, J. M.: Improved estimates of net ecosystem exchanges in mega-countries using GOSAT and OCO-2 observations, Commun. Earth Environ., 5, 737, https://doi.org/10.1038/s43247-024-01910-w, 2024.

Zhang, X., Yang, H., Bu, L., Fan, Z., Xiao, W., Chen, B., Zhang, L., Liu, S., Wang, Z., Liu, J., Chen, W., and Lee, X.: Estimation of diurnal emissions of CO_2 from thermal power plants using spaceborne integrated path differential absorption (IPDA) lidar, Atmos. Chem. Phys., 25, 6725–6740, https://doi.org/10.5194/acp-25-6725-2025, 2025.

Zhao, X., Marshall, J., Hachinger, S., Gerbig, C., Frey, M., Hase, F., and Chen, J.: Analysis of total column CO_2 and CH_4 measurements in berlin with WRF-GHG, Atmos. Chem. Phys., 19, 11279–11302, https://doi.org/10.5194/acp-19-11279-2019, 2019.

Zhao, X., Chen, J., Marshall, J.,Gałkowski, M., Hachinger, S., Dietrich, F., Shekhar, A., Gensheimer, J.,Wenzel, A., and Gerbig, C.: Understanding greenhouse gas (GHG) columnconcentrations in munich using the weather research and forecasting (WRF) model,Atmos. Chem. Phys., 23, 14325–14347, https://doi.org/10.5194/acp-23-14325-2023,2023.

https://doi.org/10.5194/egusphere-2025-6470
Preprint. Discussion started: 25 February 2026

Zong, L., Yang, Y., Xia, H., Yuan, J., and Guo, M.: Elucidating the Impacts of Various Atmospheric Ventilation Conditions on Local and Transboundary Ozone Pollution Patterns: A Case Study of Beijing, China, JGR Atmospheres, 128, e2023JD039141, https://doi.org/10.1029/2023JD039141, 2023.

615